Remmert, S. M., Banks, S. T., Harvey, J. N., Orr-Ewing, A. J., & Clary, D. C. (2011). Reduced dimensionality spin-orbit dynamics of CH3 + HCl reversible arrow CH4 Cl on ab initio surfaces. Journal of Chemical Physics, 134(20), -. [204311]. 10.1063/1.3592732

Reduced dimensionality spin-orbit dynamics of $CH_3 + HCl \rightleftharpoons CH_4 + Cl$ on ab initio surfaces.

Sarah M. Remmert,[1, a)] Simon T. Banks,[2] Jeremy N. Harvey,[3] Andrew J. Orr-Ewing,[3] and David C. Clary[1, b)]
[1)] *Department of Chemistry, University of Oxford, PTCL, South Parks Road, Oxford, OX13QZ, U.K.*
[2)] *Department of Chemistry, University College London, 20 Gordon Street, London, WC1H 0AJ, U.K.*
[3)] *School of Chemistry, University of Bristol, Bristol, BS8 1TS, U.K.*

(Dated: 11th April 2011)

A reduced dimensionality quantum scattering method is extended to the study of spin-orbit nonadiabatic transitions in the $CH_3 + HCl \rightleftharpoons CH_4 + Cl(^2P_J)$ reaction. Three two-dimensional potential energy surfaces are developed by fitting a 29 parameter double-Morse function to CCSD(T)/IB//MP2/cc-pV(T+d)Z-dk *ab initio* data; interaction between surfaces is described by geometry-dependent spin-orbit coupling functions fit to MCSCF/cc-pV(T+d)Z-dk *ab initio* data. Spectator modes are treated adiabatically via inclusion of curvilinear projected frequencies. The total scattering wavefunction is expanded in a vibronic basis set and close-coupled equations are solved via R-matrix propagation. Ground state thermal rate constants for forward and reverse reactions agree well with experiment. Multi-surface reaction probabilities, integral cross sections, and initial-state selected branching ratios all highlight the importance of vibrational energy in mediating nonadiabatic transition. Electronically excited state dynamics are seen to play a small but significant role as consistent with experimental conclusions.

I. INTRODUCTION

Reactions involving hydrogen transfer between chlorine radicals and hydrocarbon molecules are widely studied both theoretically and experimentally. In particular, the reaction processes:

$$HCl + CH_3 \longrightarrow Cl(^2P_J) + CH_4 \quad (1)$$
$$Cl(^2P_J) + CH_4 \longrightarrow HCl + CH_3 \quad (2)$$

have been the focus of intense investigation. Accurate description of reaction (2) is essential in polar atmospheric chemistry; it is a major sink for chlorine radicals and hinders competing processes which lead to the degradation of the stratospheric ozone.[1–3] Hence, knowledge of the reaction rate at low temperatures is necessary for modelling ozone depletion.[4] Conversely, the reaction can also be viewed as a major sink for the greenhouse gas methane, second to the destruction of methane via reaction with the OH radical.[5] Furthermore, it is hypothesised that reaction (2) is essential in interpreting the combustion of chlorinated hydrocarbons – a topic necessary for understanding the consequences of toxic waste incineration.[6]

In addition to its physical importance, this reaction has emerged in the laboratory as a prototype for understanding the basic principles of polyatomic reaction dynamics. Numerous sophisticated experimental and theoretical studies have been performed in recent years, designed not only to measure forward and reverse reaction rates, but to probe in detail the transfer of internal and kinetic energy for the ground state reaction. Reaction (2) is mildly endothermic[7,8] with a late (product-like) transition state.[9] C_{3v} symmetry[10,11] and a collinear angle of abstraction (Cl−H−C) are maintained along the reaction path.[7,10,12,13] Steric hindrance is expected to have a significant effect with a tight TS structure;[14] the experimental pre-exponential factor (1×10^{-11} cm^3 molecule^{-1} s^{-1}) is approximately 30 times less than that of the hard sphere collision rate.[15] Furthermore, due to the heavy-light-heavy (HLH) nature of this system, quantum effects such as oscillating reactivity and resonances govern the kinetics and dynamics.[11,16] Quasi-bound states in the TS region have been predicted[17] corresponding to HLH "chattering" of the light atom.[16] Thermal rate constant data shows significant curvature of the Arrhenius plot, further emphasizing the need for a quantum mechanical treatment.[15,18]

In general, two reaction mechanisms have been characterized.[19] Small impact parameter (b) collisions produce backwards scattered products in a rebound mechanism.[7,16] Peripheral (high b) collisions lead to a so-called "stripping" mechanism with a more forward scattered distribution,[7,16,20] especially at high collision energies.[17,21,22] Reaction (2) is preferentially enhanced by excitation in both the C–H symmetric stretch and the umbrella excitation of the CH_4 group, whereas reaction (1) is enhanced by excitation of the H–Cl vibration but decreased by umbrella excitation of the CH_3.[23–25] Intramolecular vibrational redistribution is thought to be significant;[26] the reaction path coordinate couples to the CH_4 symmetric stretch and umbrella mode in the $Cl + CH_4$ channel,[24,27] and to the H–Cl stretch and CH_3 bending modes in the $HCl + CH_3$ channel.[27] One would expect coupling between bending and stretch motions to significantly influence the reaction.

Though studies have primarily focused on the ground state, several recent experiments have investigated the

[a)] Electronic mail: smremmert@gmail.com
[b)] Electronic mail: david.clary@chem.ox.ac.uk

role of nonadiabatic processes involving the spin-orbit state $Cl(^2P_{\frac{1}{2}})$. Liu et al. have characterized the reactions $Cl(^2P_{\frac{1}{2}})$ $+CH_4$[28] and $Cl(^2P_{\frac{1}{2}})$ $+CH_2D_2$,[29] confirming the small but significant contribution to reaction of spin-orbit excited states[29] and noting in both studies the production of vibrationally excited HCl ($\nu = 1$). Orr-Ewing and coworkers have instead quantified production of $Cl(^2P_{\frac{1}{2}})$ from the reaction CH_3+HCl;[30–33] the nonadiabatic branching ratio was found to be $\Gamma = 0.14\pm0.02$ (at an average collision energy of 22.3 kcal mol^{-1}).[32] Both forward and reverse experiments indicated a two-step mechanism for nonadiabatic transition, leading to similar dynamics for ground and excited state processes.[28,31] Direct comparison between these experiments is difficult given different initial vibrational distributions; experiments for $CH_3 + HCl$ contain umbrella excited CH_3 radicals with a vibrationally cold HCl distribution, whereas the experiments probing reaction (2) yield stretch excited HCl.

Nonadiabatic effects in triatomic $X + H_2$ reactions have been well characterized (X=Cl,[34–39] X=F,[40–43] X=Br[44–46]). Generally, $X(^2P_{\frac{1}{2}}) + H_2$ reactions were found to be a small but significant reaction pathway, accounting for approximately 10% ($Cl^{35,37}$), 10-25% ($F^{40,41}$), or 10-40% ($Br^{44,46}$) of total reactivity. Several studies also noted the release or excitation of one quantum of H–H stretch associated with nonadiabatic transition.[45,46]

Multiple-surface quantum scattering studies of polyatomic collisions have been rare due to computational limitations; investigation of atom + molecule systems such as $O(^3P) + CH_3 \longrightarrow CH_3O$ have required reduced dimensionality (RD) approximations and surface coupling simplifications to achieve computational feasibility.[47] Despite the detailed experimental work for the title reaction, to the best of our knowledge no multi-surface characterisation has been performed, leaving several remaining questions regarding nonadiabatic properties. The extent and location of nonadiabatic transition, the mechanism of nonadiabatic coupling and the role of vibrational motion in mediating nonadiabatic reaction are all addressed in this study in an attempt to bridge the gap between forward and reverse experimental results.

A full dimensional treatment of the title reaction would be challenging for a ground state study, but the problem becomes prohibitively large in considering multiple electronic surfaces. The current approach makes use of a two-dimensional time-independent quantum scattering method derived from the bending corrected rotating linear model (BCRLM) of Walker and Hayes,[48] combined with an analytical potential energy surface (PES) fit to high-level *ab initio* data.[49] Internal degrees of freedom (DOF) are divided into two *active* modes explicitly treated in the quantum scattering, and $3N-8$ *spectator* modes, which are approximately treated via inclusion of curvilinear-projected zero-point energies (ZPE) in the PES.[50,51] Variants of this approach have been successfully applied to a number of ground state reactions,[49,52–56] including $Cl + CH_4 \rightarrow HCl + CH_3$.[11] In this paper, the method is extended to include multi-surface characterization of nonadiabatic transitions.

This paper is organized as follows. In section II, the multi-surface reaction model is discussed in the diabatic representation and the hyperspherical coordinate system is introduced. In section III, the energetic properties, *ab initio* calculations, and development of potential energy surfaces are discussed. Section IV presents the solution of the quantum scattering equations while sections V and VI discuss scattering in the single and multi-surface representations, respectively. General conclusions are given in section VII.

II. BACKGROUND THEORY

A. Approximate diabatic representation

Diabatic and adiabatic representations may be used to solve multi-surface time-independent quantum scattering problems, differing in the choice of electronic basis set.[57] The diabatic representation involves choosing electronic basis functions such that the nonadiabatic coupling terms in the kinetic energy operator (KEO) are sufficiently small in comparison to the coupling in the electronic Hamiltonian that they can be neglected in scattering calculations.[58] This advantage is countered by the difficulty in obtaining diabatic surfaces, which must be generated by a non-unique unitary transformation of the adiabatic potentials.[57] In a detailed diabatic representation, off-diagonal coupling terms include all nuclear and electronic angular momenta couplings, such as spin-orbit, electronic, rotational, and Coriolis couplings.[59] In the current study an approximate diabatic basis is implemented by assuming spin-orbit coupling (SOC) dominates the coupling terms.[58] This results in a potential matrix where the diagonal terms are the spin-free electronic energies and the off-diagonal terms are the SOC constants, both of which can be generated from *ab initio* calculations. Hereafter all references to the diabatic representation refer to this approximate approach.[58]

B. Multi-surface reaction model

The title reaction system contains three, two-fold degenerate potential energy surfaces (PES); the two-fold degeneracy arises from the spin states of the unpaired electron in the valence p orbital of the Cl radical. In the diabatic, C_{3v} symmetric representation, all three states are degenerate in the asymptotic limit of infinite separation of the Cl atom from methane. The ground state reaction occurs along the doubly-degenerate A_1 potential ($1A'$ in C_s symmetry). The four-fold degenerate E potential ($2A' + 1A''$ in C_s symmetry) correlates instead to excited state $HCl + CH_3$, which are sufficiently high in

energy to be negligible in the study of low to moderate collision energy dynamics. Complexity arises when SOC splits the degeneracy of the asymptotic states into the four-fold degenerate Cl ($^2P_{\frac{3}{2}}$) ground state and the two-fold degenerate ($^2P_{\frac{1}{2}}$) excited state, as shown in Figure 1. In the asymptotic limit, the splitting between the states equals $\Delta E_{SOC} = 882$ cm^{-1}, the spin-orbit splitting of the Cl atom.[60] The two lower diabatic surfaces decrease by 1/3 of ΔE_{SOC}, whereas the upper state increases by 2/3 of the same value. Due to this energy splitting, any reaction from (to) Cl ($^2P_{\frac{1}{2}}$)+ CH_4 to (from) ground state HCl+CH_3 must involve a nonadiabatic transition, which occurs in the Cl + CH_4 channel. A primary interest of multi-surface scattering calculations is understanding these nonadiabatic interactions. (In all subsequent discussions, Cl ($^2P_{\frac{1}{2}}$) will be abbreviated as Cl*; Cl ($^2P_{\frac{3}{2}}$) as Cl.)

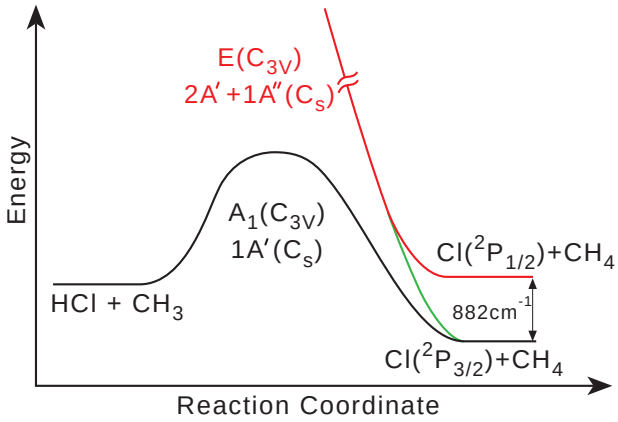

Figure 1. Diagram of the three HCl + CH_3 ⇌ Cl + CH_4 potential energy surfaces as a function of reaction coordinate. The two excited states in the diabatic representation break degeneracy due to spin-orbit coupling in the adiabatic representation, leading to a four fold degenerate ground state and a two fold degenerate excited state split by 882 cm^{-1}.

C. Hyperspherical Coordinates

Hyperspherical coordinates are used, allowing for a smooth description of the reaction surface from reactants to products without requiring coordinate matching procedures.[61–64] These coordinates are particularly suited to the study of HLH systems, which are characterized by large skewing angles with greater separability of motion between the ρ and δ coordinates.[65]

Product Jacobi coordinates are defined by approximating Cl + H−C−H_3 as a pseudo tetra-atomic system: R is defined as the centre of mass (COM) distance between fragments Cl-H and CH_3, while r is the distance between Cl and the abstracted atom, H_a (Figure 2(a)). For large separations, R roughly corresponds to the translational motion of the HCl towards CH_3, whereas the r correlates to the vibrational motion of the H−Cl bond. The reduced mass definitions

$$\begin{aligned} M_1 &= m_{HCl} m_{CH_3}/m_{tot} \\ M_2 &= m_{Cl} m_{H_a}/m_{H_aCl} \\ M_3 &= m_C m_{H_3}/m_{CH_3} \\ \mu &= (M_1 M_2 M_3)^{1/3} \end{aligned} \tag{3}$$

are used to define the hyperspherical radius, ρ and angle, δ by[11,49,55,66]

$$\frac{M_1}{\mu} R^2 = [\rho \cos(\delta)]^2 \tag{4}$$

$$\frac{M_2}{\mu} r^2 = [\rho \sin(\delta)]^2 . \tag{5}$$

The maximum value of the hyperangle (skewing angle) is defined according to

$$\delta_{max} = \tan^{-1}\left[\sqrt{\frac{m_{H_a} m_{tot}}{m_{Cl} m_{CH_3}}}\right] . \tag{6}$$

Large δ values correspond to the Cl+CH_4 channel; small δ values the CH_3 + HCl channel.

III. SYSTEM ENERGETICS

A. Basis Set Tests

Basis set tests were performed in order to determine the most appropriate method for development of the ground and excited state diabatic PESs (Table I). All *ab initio* calculations in this study were performed using the Molpro electronic structure package.[67] Geometry calculations were performed at the MP2 level of theory; CCSD(T) was used for single point energy calculations, with correlation consistent basis sets cc-pV(X+d)Z-dk (X = T, Q), where (+d) indicates additional *d*-polarization functions for the Cl atom[68,69] and (-dk) refers to the use of Douglas-Kroll scalar relativistic basis sets. In Table I, basis sets are indicated by order X//X′, where geometries were computed at the X′ level with X energy corrections, and where [T,Q]//X notation indicates geometries at the X level with two-point (T-Q) basis set extrapolated energies determined via the method of Halkier et al.[70]

In general, it was found that increasing the order of the basis set decreases the forward and reverse barrier heights and reaction energies. The Q//T vibrationally corrected reverse reaction barrier height (3.57 kcal mol^{-1}) compares favorably to CCSD(T)/aug-cc-pVTZ and CCSD(T)/aug-cc-pVQZ//CCSD(T)/aug-cc-pVTZ results of Troya et al.,[71] which were found to be 3.64 and 3.06 kcal mol^{-1}, respectively. Geometry calculations with a Q basis were prohibitively expensive for surface development. Therefore, *ab initio* surfaces were

Table I. Basis set tests for reaction $HCl + CH_3 \rightleftharpoons Cl + CH_4$. CCSD(T) relative energies in kcal mol^{-1}; vibrationally corrected barrier heights shown in parentheses.

Series[a]	ΔV_r	ΔE	ΔV_f
T//T	9.41 (5.12)	-7.04 (-1.92)	2.37 (3.19)
Q//Q	7.86 (3.80)	-5.93 (-1.08)	1.93 (2.72)
Q//T	7.86 (3.57)	-5.92 (-0.79)	1.96 (2.78)
[T, Q]//T	6.88 (2.57)	-5.33 (-0.21)	1.55 (2.37)
[T, Q]//Q	6.86 (2.80)	-5.34 (-0.48)	1.52 (2.32)

[a] ΔV_r is the reverse barrier height, ΔE is the reaction energy (products – reactants) and ΔV_f is the forward barrier height. Numbers in parentheses indicate zero-point corrected energies.

Table II. TS geometric parameters at MP2/cc-pV(T+d)Z-dk level of theory. Stationary point moments of inertia in amu×$bohr^2$

Parameter	Bond length / nm	Parameter	Angle
Cl–H_a	1.45	C–H_a–Cl	180°
H_a–C	1.36	H–C–H	116.1°
H–C	1.08	H–C–H_a	101.6°
Species	I_a	I_b	I_c
CH_3	6.23	6.23	12.46
HCl	5.67		
TS	12.10	314.65	314.65

generated using both Q//T and [T,Q]//T (infinite basis, hereafter abbreviated IB) levels of theory, which provided reasonable compromises between computational efficiency and accuracy.

B. Stationary Points

Ground state stationary point geometries and frequencies were calculated at the MP2-cc-pV(T+d)Z-dk level of theory. The transition state (TS) and reactant/product geometries are shown in Figures 2(a) and 2(b), respectively; it was found that the reactant and product bond lengths accurately reproduce experimental values.[72,73] TS geometries and stationary point moments of inertia are given in Table II; the TS possesses a collinear geometry as consistent with the assumptions of this study (Figure 2(a)). Intrinsic reaction coordinate (IRC) calculations performed at the same level of theory also confirmed the presence of a collinear, C_{3v} symmetric reaction path. Stationary point frequencies are given in Table III.

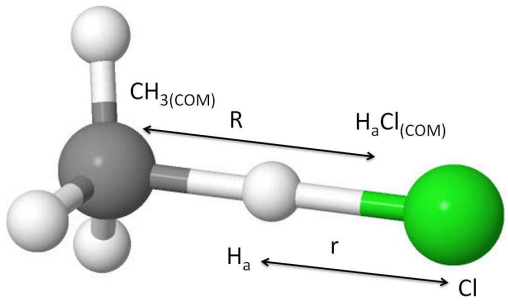

(a)Transition state geometry.

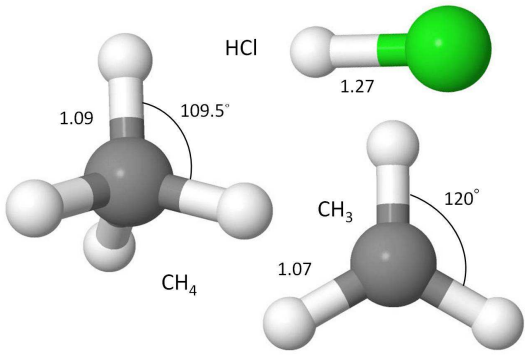

(b)Reactant and product geometries.

Figure 2. $HCl + CH_3 \rightleftharpoons Cl + CH_4$ stationary point geometries and Jacobi coordinate definition. Bond lengths given in Å.

C. Grid Development and Frequency Projection

A grid of *ab initio* data for the PES was generated by performing partial geometry optimizations at MP2/cc-pV(T+d)Z-dk level of theory, where bond lengths pertaining to the active coordinates (H_a–C and Cl–H_a) were held fixed and spectator DOF were allowed to relax. Frequency calculations were performed at each grid point. Ground state (A_1) frequencies were assumed to be valid for the excited E surfaces in the $Cl + CH_4$ channel, where behavior on both diabatic surfaces should be very similar. Preliminary tests showed that the reaction maintained a collinear Cl–H_a–C angle across the grid, and therefore C_{3v} symmetry was enforced in the calculations. Data points were computed from $\delta_{min} = 0$ to δ_{max} and from $\rho \sim 7$ au to $\rho \sim 21$ au. Hyperspherical coordinates were recomputed following COM changes post-optimization. Due to the different symmetries of the ground (A_1/A') and excited (E/A'') electronic states, energy corrections were performed using single reference approaches: CCSD(T)/IB and CCSD(T)/cc-pV(Q+d)Z-dk. Surfaces were generated for both *ab initio* methods; the majority of the results presented in this paper were generated with the higher level IB surface.

Spectator modes were treated approximately via ad-

Table III. Harmonic frequencies for stationary points at the MP2/cc-pV(T+d)Z-dk level, in cm^{-1}. Transition state frequencies are given prior to (pre) and following (post) curvilinear projection of explicitly treated vibrational modes.

CH_3	HCl	CH_4	TS (pre)	TS (post)
486.0	3054.3	1349.6	1232.5i	
1445.4		1349.7	324.5	324.5
1445.7		1349.7	334.1	336.7
3177.9		1586.3	512.1	
3368.7		1586.4	959.4	888.1
3368.7		3075.7	965.3	965.3
		3211.3	1214.0	973.3
		3211.3	1442.7	1433.7
		3211.3	1446.6	1446.6
			3127.0	3113.9
			3294.7	3294.7
			3296.3	3296.2

dition of zero-point energy to the potential; the spectator mode ZPE was determined by projecting the two active modes from the Hessian prior to diagonalization. Previous studies have shown that the curvilinear projection method[50,51] is an improvement upon the rectilinear scheme;[74] the latter was shown to result in the unphysical loss of vibrational energy due to the introduction of large post-projection imaginary frequencies.[50,51] Both methods were implemented in the current study; curvilinear coordinates were defined in terms of 5 bonds, 5 angles, and one doubly-degenerate linear angle bend. The curvilinear method was chosen as it significantly reduced the number of post-projection imaginary frequencies, though some remained and were set to zero. Curvilinear projection of the TS frequencies is shown in Table III.

The active modes are the reaction coordinate at $1232i$ cm^{-1}, (hydrogen chattering of the transferring hydrogen with some umbrella-like bending motion of the CH_3 group) and the mode at 512 cm^{-1} (heavy atom breathing of the Cl and CH_3 groups). There is a small degree of coupling between the spectator and active modes as observed by post-projection decrease of the modes at 1214, 959.4, 3296.3 and 3127 cm^{-1} by 19.8%, 7.4%, 0.6% and 0.4%, respectively, amounting to a loss of 334.1 cm^{-1} of vibrational energy at the TS. The largest coupling is due to the umbrella mode at 1214 cm^{-1} and it is likely that this coupling remains important along the reaction path.

D. Potential Energy Surfaces

The potential matrix, $\mathbf{V}(\rho,\delta)$, is constructed from four *ab initio* surfaces, namely the ground diabatic state $V^{\rm d}_{\rm A_1}(\rho,\delta)$, the degenerate excited diabatic states $V^{\rm d}_{\rm E}(\rho,\delta)$, the SOC potential between the A_1 and E states (A), and the SOC between the degenerate E states (B).

Diagonalization of the potential matrix at each geometry (indicated below by an arrow) yields eigenvalues corresponding to the ground ($V^{\rm ad}_{\rm A_1}$) and excited ($V^{\rm ad}_{\rm E_{low}}$, $V^{\rm ad}_{\rm E_{high}}$) adiabatic potential surfaces that explicitly include the effects of SOC. SOC increases the reverse barrier height of $V^{\rm ad}_{\rm A_1}$ relative to $V^{\rm d}_{\rm A_1}$, and splits the degeneracy of the excited diabatic surfaces into $V^{\rm ad}_{\rm E_{low}}$ and $V^{\rm ad}_{\rm E_{high}}$, which correlate asymptotically to Cl + CH_4 and Cl* + CH_4, respectively.

$$\mathbf{V}(\rho,\delta)=\begin{bmatrix} V^{\rm d}_{\rm A_1} & {\rm A} & {\rm A} \\ {\rm A} & V^{\rm d}_{\rm E} & {\rm B} \\ {\rm A} & {\rm B} & V^{\rm d}_{\rm E} \end{bmatrix} \longrightarrow \begin{bmatrix} V^{\rm ad}_{\rm A_1} & 0 & 0 \\ 0 & V^{\rm ad}_{\rm E_{low}} & 0 \\ 0 & 0 & V^{\rm ad}_{\rm E_{high}} \end{bmatrix}$$

1. Diabatic surfaces.

Diabatic potential energy surfaces were constructed by fitting the following analytical 29-parameter double-Morse function to *ab initio* spin-free electronic energies and spectator ZPE corrections:

$$\begin{aligned} V(\rho,\delta) = {} & f_1\left[(1-\exp(g_1\delta+h_1))^2-c_{14}\right] \\ & + \; f_2\left[(1-\exp(-(g_2\delta+h_2)))^2-c_{28}\right]+c_{29} \end{aligned} \tag{7}$$

where

$$f_1 = (1+c_1\rho^{c_2}\exp(c_3\rho))c_4 \tag{8}$$
$$f_2 = (1+c_{15}\rho^{c_{16}}\exp(c_{17}\rho))c_{18} \tag{9}$$
$$g_1 = c_5+c_6\rho+c_7\rho^2 \tag{10}$$
$$g_2 = c_{19}+c_{20}\rho+c_{21}\rho^2 \tag{11}$$
$$h_1 = c_8+c_9\rho+c_{10}\rho^2-\log(c_{11}+c_{12}\rho+c_{13}\rho^2) \tag{12}$$
$$h_2 = c_{22}+c_{23}\rho+c_{24}\rho^2+\log(c_{25}+c_{26}\rho+c_{27}\rho^2). \tag{13}$$

Initial parameters for the A_1 fit were taken from reference,[11] adjusted for high energy limits and modified by a nonlinear least squares regression (lsqcurvefit in Matlab[75]). The surface fitting toolbox[75] was used to identify outliers for low-energy fitting. Parameters for the E surfaces were similarly determined. To reproduce the *ab initio* degeneracy of the A_1 and E surfaces in the asymptotic Cl+CH_4 channel, asymptotic grid points (0.21 rad $< \delta <$ $\delta_{\rm max}$; 14 au $< \rho <$ 21 au) evaluated from the final A_1 surface were included in the fit. E surfaces were fit for 0.16 rad $< \delta <$ $\delta_{\rm max}$, but for $\delta <$ 0.16 rad extend smoothly to collision energies too high to be of influence in the current study. The parameters for the A_1 and E surfaces are given in Table IV; the surfaces are valid for $8 \le \rho \le 16$ au.

The main results of this study are presented for the IB surface. The $V^{\rm d}_{\rm A_1}$ TS slightly favors the HCl + CH_3 channel and there is evidence of shallow van der Waals minima, especially in the Cl + CH_4 channel. A contour diagram of the overlap of $V^{\rm d}_{\rm A_1}$ and $V^{\rm d}_{\rm E}$ shows that the excited diabatic states are much higher in energy than

Table IV. PES parameters for the IB and the Q//T surfaces. The number of *ab initio* grid points (#) and the sum of squared residuals (SSR / au^2) are given for each surface. The total number of grid points including evaluated data is shown in parenthesis.

	A_1(IB)	E (IB)	A_1 Q//T	E Q//T
c_1	33.5333456	34.1142578	33.7091791	33.7104657
c_2	-9.5184794	-9.6565197	-9.4137823	-9.4985922
c_3	-0.2885825	-0.2942490	-0.2984860	-0.3120208
c_4	0.3394559	0.5232066	0.3408111	0.4585513
c_5	21.5331673	18.1823482	21.8665166	18.6354881
c_6	-0.5922270	-0.1850375	-0.6199417	-0.1178949
c_7	0.0472629	0.0311757	0.0475726	0.0287326
c_8	3.9444163	4.5762280	3.8801101	4.6419913
c_9	0.1981337	0.0718168	0.2009703	0.0489267
c_{10}	-0.0127305	-0.0080245	-0.0127017	-0.0072190
c_{11}	52.6235649	53.4881748	52.8669116	53.3500438
c_{12}	251.7135322	253.0952975	252.1119879	252.6919904
c_{13}	28.8394669	17.5819660	27.9679782	21.1239275
c_{14}	12.6212925	17.6890044	12.6352265	16.1588000
c_{15}	133.5273496	135.5749067	133.4455751	135.0406265
c_{16}	-5.4643681	-5.3084698	-5.4623009	-4.9110332
c_{17}	0.2449930	0.1591238	0.2436439	0.0536798
c_{18}	0.3523492	0.5038674	0.3520120	0.4571251
c_{19}	12.3022295	16.7745072	12.9251918	17.4120445
c_{20}	0.9458117	-0.1866372	0.8651841	-0.1331262
c_{21}	-0.0257643	-0.0025329	-0.0228559	-0.0119515
c_{22}	-7.2062625	-7.1338497	-7.5700022	-6.8890311
c_{23}	-0.0440650	-0.1633082	-0.0180181	-0.1982455
c_{24}	0.0033420	0.0033680	0.0019791	0.0066089
c_{25}	-88.3174186	-83.5555132	-87.2670480	-83.8842875
c_{26}	31.8401457	42.0927039	34.5437230	42.2120505
c_{27}	-0.8966595	1.6035693	-0.8172033	0.3440478
c_{28}	-122.3617359	-120.3096212	-122.9947167	-121.4651824
c_{29}	-540.7761851	-553.1711714	-540.9150587	-549.8423194
#	171 (171)	142 (585)	171 (171)	142 (585)
SSR	2.2×10^{-4}	2.2×10^{-3}	2.2×10^{-4}	1.6×10^{-3}

the ground state before the TS is reached, indicating that nonadiabatic transition is likely to be restricted to the $Cl + CH_4$ channel (Figure 3).

2. *Spin-orbit Coupling Potentials.*

The geometry-dependent SOC terms were calculated as perturbations to the spin-free Hamiltonian at the MCSCF/cc-pV(T+d)Z-dk level of theory in Molpro[67] and scaled by the ratio of the experimental[60] to *ab initio* SOC for the Cl atom (1.05687). The *ab initio* SOC terms were found to remain fairly constant across the $Cl + CH_4$ channel but to decrease quickly with δ and ρ in the interaction region. A was found to change more as a function of geometry than B; the 8-parameter analytical function

$$A/B(\rho,\delta) = \frac{c_1}{(c_2\rho + c_3\delta)^C} + c_8 \qquad (14)$$
$$C = (c_4 + c_5\delta + c_6\delta^2 + c_7\rho)$$

was fit to *ab initio* data for both constants for 0.15 rad $\leq \delta \leq \delta_{max}$ via nonlinear least squares regression (lsqcurvefit in Matlab[75]). For $\delta \leq 0.15$ rad, the functions were set to zero, reflecting the abrupt decrease in magnitude of the *ab initio* constants. This discontinuity has negligible effect. The diabatic excited state is much higher in energy than the ground state at this geometry making the possibility of a transition highly unlikely. The A and B surface parameters are given in Table V.

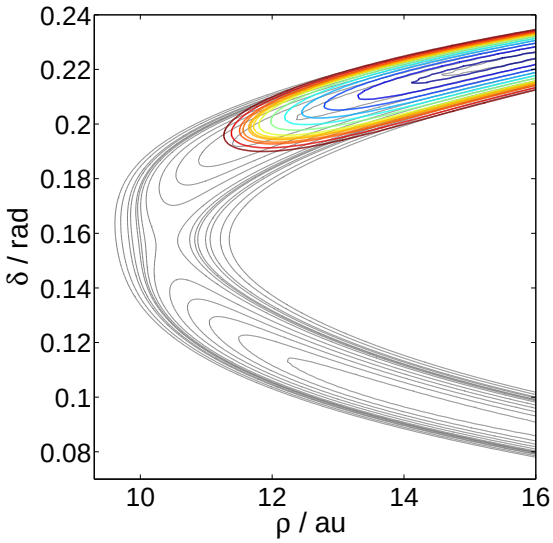

Figure 3. Contour diagram of ground A_1 (gray) and excited E (color) diabatic states for reaction $HCl + CH_3 \rightleftharpoons Cl + CH_4$, computed from the basis set extrapolated surface model. Large δ corresponds to the $Cl+CH_4$ reactant channel; small δ the $HCl+CH_3$ channel. The surfaces are asymptotically degenerate but diverge in the interaction region, where the highest E contour lies 0.35 eV above the corresponding A_1 contour.

3. *Surface characterisation.*

The minimum energy path (MEP) of the six diabatic and adiabatic surfaces in the $Cl+CH_4$ channel is shown as a function of ρ in Figure 4, for the IB surface. The final sector (ρ = 16 au) diabatic surfaces are approximately degenerate as consistent with the model. Relative to the $V^{d}_{A_1}$ potential, $V^{ad}_{A_1}$ and $V^{ad}_{E_{low}}$ are on average shifted down by ∼1/3 (263 cm^{-1}) of the SO splitting, $V^{ad}_{E_{high}}$ is shifted up by ∼2/3 of the same value (588 cm^{-1}) and the average splitting due to SOC is 852 cm^{-1}. This splitting is close to the experimental splitting value for the Cl atom (882 cm^{-1}).[60]

Table V. SOC surface parameters. Powers of 10 in parentheses. The number of *ab initio* grid points (#) and the sum of squared residuals (SSR / au^2) are given for each surface.

	A	**B**
c_1	1.0278043(-4)	1.7837221(-5)
c_2	1.6730222(-1)	8.8885700(-2)
c_3	1.9180895	1.1052732
c_4	-7.6335945(-1)	-4.0910503(+1)
c_5	-1.1925541(+2)	4.1022580(+2)
c_6	6.2782817(+2)	-8.8115621(+2)
c_7	2.8241506(-1)	3.6444004(-3)
c_8	1.2686625(-3)	1.3401619(-3)
#	199	199
SSR	2.1×10^{-9}	9.0×10^{-11}

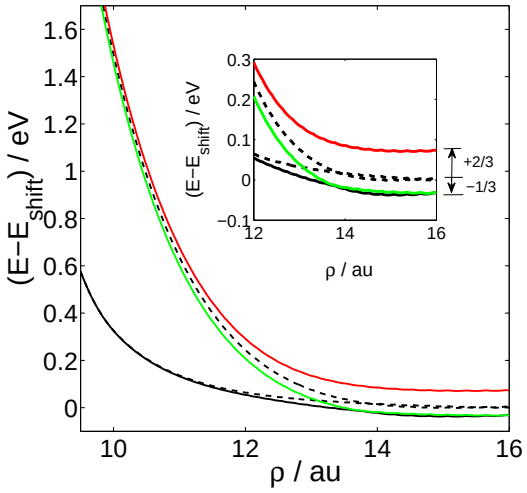

Figure 4. Minimum energy path for the diabatic and adiabatic basis set extrapolated surfaces in Cl + CH_4 channel. Spin orbit splitting for the adiabatic surfaces (-1/3, +2/3) shown for the asymptotic region in the inset. Diabatic surfaces (black, dashed); adiabatic surfaces: $V^{\rm ad}_{\rm A_1}$ (black, solid), $V^{\rm ad}_{\rm E_{low}}$(green), $V^{\rm ad}_{\rm E_{high}}$(red).

The surface barrier heights ($\Delta V_{r/f}$), energy of reaction (ΔE), the depth of the vdW wells relative to asymptotic limits ($E_{r/p} - E_{vdW,r/p}$), and the barrier heights relative to the vdW wells ($\Delta V_{r/f,vdW}$) are given in Table VI for the $V^{\rm ad}_{\rm A_1}$ and $V^{\rm d}_{\rm A_1}$ IB surfaces (where the labels "r" and "p" designate CH_3 + HCl and Cl + CH_4, respectively). The surface barrier heights include the effects of spectator mode vibrations and are therefore not directly comparable to *ab initio* results. The forward barrier height is very similar for both surfaces but the reverse barrier height is much higher on the adiabatic surface, indicating that though SO effects do not significantly contribute to changes in the CH_3 + HCl channel or at the TS, SO effects are large in the Cl + CH_4 channel. In addition, the TS saddle point (ρ = 10.40 au, δ = 0.16 rad) is similar

Table VI. Energetic properties of ground state diabatic and adiabatic IB surfaces for reaction HCl + $CH_3 \rightleftharpoons$ Cl + CH_4. Energies given in kcal mol^{-1}.

	$V^{\rm d}_{\rm A_1}$	$V^{\rm ad}_{\rm A_1}$
ΔV_f	6.11	6.09
ΔV_r	6.73	7.47
ΔE	-0.62	-1.38
$E_r - E_{vdW,r}$	0.25	0.25
$E_p - E_{vdW,p}$	0.01	0.12
$\Delta V_{f,vdW}$	6.36	6.34
$\Delta V_{r,vdW}$	6.74	7.59

to the *ab initio* determined value (ρ = 10.24 au, δ = 0.16 rad), providing evidence that the surface accurately reproduces *ab initio* properties.

IV. SCATTERING THEORY

A. Scattering equations and R-matrix propagation

The BCRLM Hamiltonian (scaled by $\rho^{-3/2}$)[48] for multi-surface scattering is given in atomic units according to

$$H = -\frac{1}{2\mu}\frac{\partial^2}{\partial\rho^2} - \frac{1}{2\mu\rho^2}\frac{\partial^2}{\partial\delta^2} + \frac{3}{8\mu\rho^2} + \frac{\hat{J}^2}{2\mu\rho^2} + H_{\rm el}, \quad (15)$$

where $H_{\rm el}$ is the electronic Hamiltonian and where a collinear reaction angle and linear rigid rotor treatment of total angular momentum are assumed ($\hat{J}^2 = J(J+1)$). The scattering problem is solved via the inelastic R-matrix propagation method of Stechel et al.,[76] implemented instead of the reactive version due to the use of hyperspherical coordinates.[76,77] R-matrix propagation is an iterative algorithm that divides the reaction surface into even width (h_m) sectors of the scattering coordinate ρ. Within each ρ-sector m, the total scattering wavefunction for quantum state $k = (i, \nu)$ is expanded in a *vibronic* basis[78] of products of the diabatic (Φ^d_i for electronic state i) and vibrational ($\chi_{(i,\nu)}$ for vibrational state ν) basis functions:

$$\Psi_k(\rho, \delta; \rho_m) = \sum_{k'}^{N} f_{k'k}(\rho; \rho_m)\Phi^d_{i'}\chi_{(i,\nu)'}(\delta; \rho_m). \quad (16)$$

The primitive basis $\{\chi_{(i,\nu)}\}$ is comprised of one-dimensional discrete variable representation (DVR) basis functions, constructed according to the fixed-node DVR basis of Muckerman et al.[79] This basis allows for the efficient, analytical construction of δ-dependent Hamiltonian matrix elements; for each electronic state i, the basis functions $\chi_{(i,\nu)}(\delta; \rho_m)$ retain the Kronecker delta property $\langle\chi_{(i,\nu)}|\chi_{(i,\nu)'}\rangle = \delta_{\nu\nu'}$.

The close-coupled equations are second order linear differential equations in the scattering coordinate ρ, constructed by applying the Hamiltonian in equation (15) to the total scattering wavefunction:

$$\frac{d^2}{d\rho^2} f_{(i,\nu)} + \sum_{(i,\nu)'} f_{(i,\nu)'(i,\nu)} W_{(i,\nu)(i,\nu)'} = 0, \tag{17}$$

where $f_{(i,\nu)'(i,\nu)}(\rho) = f_{k'k}(\rho)$ are the translational scattering functions. Elements of the coupling matrix $\mathbf{W}$ are given according to

$$W_{(i,\nu)(i,\nu)'} = 2\mu \left[\delta_{ii'} \langle \chi_{(i,\nu)} | \frac{1}{2\mu\rho^2} \frac{\partial^2}{\partial \delta^2} | \chi_{(i,\nu)'} \rangle \right. \tag{18}$$
$$\left. + \left(E_{(i,\nu)} - \frac{3}{8\mu\rho^2} - \frac{J(J+1)}{2\mu\rho^2} \right) \delta_{ii'} \delta_{\nu\nu'} + V_{ii'} \delta_{\nu\nu'} \right],$$

where $E_{(i,\nu)}$ is the total energy and where the final term in the coupling matrix element reflects the fact that $H_{\rm el}$ acts upon the diabatic wavefunctions to yield the diabatic ($V_{ii'},\ i = i'$) or coupling ($V_{ii'},\ i \neq i'$) potentials. The number of close-coupled equations reflects the number of energetically accessible vibronic states at a particular collision energy for the two active DOF.[80] The Schrödinger equation is equivalently and more intuitively constructed in vector form:[46]

$$T \begin{pmatrix} \Psi_{1\nu} \\ \Psi_{2\nu} \\ \Psi_{3\nu} \end{pmatrix} + \begin{pmatrix} V^{\rm d}_{\rm A_1} & \rm A & \rm A \\ \rm A & V^{\rm d}_{\rm E} & \rm B \\ \rm A & \rm B & V^{\rm d}_{\rm E} \end{pmatrix} \begin{pmatrix} \Psi_{1\nu} \\ \Psi_{2\nu} \\ \Psi_{3\nu} \end{pmatrix} = E \begin{pmatrix} \Psi_{1\nu} \\ \Psi_{2\nu} \\ \Psi_{3\nu} \end{pmatrix}.$$

In solving the close-coupled equations, transformation from the primitive coupled basis ($\left\{\Phi^d_i \chi_{(i,\nu)}\right\}$) to the target vibronic basis ($\{\phi_{(i,\nu)}\}$) where off-diagonal coupling is removed must be performed in the center of each sector. The new target basis is expressed as an expansion in the primitive DVR basis as

$$\phi_k(\delta; \rho_m) = \sum_{k'} T^m_{k'k} \Phi^d_{i'} \chi_{k'}(\delta; \rho_m). \tag{19}$$

This transformation is equivalent to diagonalizing $\mathbf{W}$ (assumed to be constant across the width of each sector):

$$\mathbf{T}^{mT} \mathbf{W}(\rho_m) \mathbf{T}^m = \lambda^2(m), \tag{20}$$

where $\mathbf{T}$ is an orthogonal matrix of the expansion coefficients of the scattering wavefunction in the primitive basis and $\lambda^2(m)$ is a diagonal matrix containing the sector-dependent eigenvalues (λ^2_k) of the coupling matrix, that are needed to construct the R-matrix recursion.

The global $N \times N$ R-matrix (the ratio of the translational functions to their outward normal gradients at each right sector boundary) is initiated in the first sector as

$$R^{(1)}_{jk} = \delta_{jk} |\lambda_j|^{-1}. \tag{21}$$

Within each subsequent sector, the elements of the local $2N \times 2N$ R-matrix $\mathbf{r}^{(m)}$ are given by

$$(r^{(m)}_1)_{jk} = (r^{(m)}_4)_{jk} = \delta_{jk} \begin{cases} |\lambda_j|^{-1} \coth |h_m \lambda_j|, & \lambda_j^2 < 0 \\ -|\lambda_j|^{-1} \cot |h_m \lambda_j|, & \lambda_j^2 \geq 0 \end{cases}$$

$$(r^{(m)}_2)_{jk} = (r^{(m)}_3)_{jk} = \delta_{jk} \begin{cases} |\lambda_j|^{-1} \mathrm{csch} |h_m \lambda_j|, & \lambda_j^2 < 0 \\ -|\lambda_j|^{-1} \csc |h_m \lambda_j|, & \lambda_j^2 \geq 0 \end{cases}.$$

Continuity of the translational functions and their derivatives at the boundary between sectors $m-1$ and m is enforced by the orthogonal transformation matrix[81]

$$\mathcal{T}(m, m-1) = \mathbf{T}^{mT} \mathcal{O}^{m,m-1} \mathbf{T}^{(m-1)}, \tag{22}$$

where $\mathbf{T}$ is given by equation (20) and the basis function overlap $\mathcal{O}^{m,m-1}$ is a unit operator for the normalized and unchanging DVR basis. Propagation from sector $m-1$ to m is achieved as follows: the transformation matrix $\mathcal{T}(m, m-1)$ is used in combination with the new sector R-matrix $\mathbf{r}^{(m)}$ and the old global R-matrix $\mathbf{R}^{(m-1)}$ to construct the new global R-matrix in sector m as

$$\mathbf{R}^m = \mathbf{r}^m_4 - \mathbf{r}^m_3 \mathbf{Z}^m \mathbf{r}^m_2, \tag{23}$$

where

$$\mathbf{Z}^m = \left[\mathbf{r}^m_1 + \mathcal{T}_{m,m-1} \mathbf{R}^{m-1} \mathcal{T}^T_{m,m-1} \right]^{-1}. \tag{24}$$

R-matrix propagation proceeds to the asymptotic region, where approximate boundary conditions are applied directly in hyperspherical coordinates in the uncoupled representation to extract the S-matrix. In this representation, the asymptotically diagonal states correlate with the adiabatic ones and thus transitions between diabatic states $k \rightarrow k'$ may be interpreted as electronic transitions between adiabatic states. To avoid oscillations in the reaction probability associated with inexact asymptotic separability of ρ and δ, boundary conditions were applied over a number of asymptotic sectors and probability matrix elements were averaged.[82,83] Previous studies reported a negligible effect of using this approximate sector averaging approach on Cl+CH_4 thermal rate constants.[84]

Incident and outgoing wavefunctions are assumed to resemble exactly out of phase plane waves in ρ and the S-matrix is extracted as

$$\mathbf{S}^J(E; n) = \left[\mathbf{R}(\rho_n) \mathbf{O}'(\rho_n) - \mathbf{O}(\rho_n) \right]^{-1} \times \left[\mathbf{R}(\rho_n) \mathbf{I}'(\rho_n) - \mathbf{I}(\rho_n) \right], \tag{25}$$

where n corresponds to a ρ-sector in the asymptotic region, $\mathbf{S}^J(E; n)$ is the energy and sector-dependent S-matrix for a particular total angular momentum value J, and the incident ($I_{kk'}$) and outgoing ($O_{kk'}$) wavefunctions for each E, J, and sector n depend upon the square root of the coupling matrix elements in the diagonal representation (λ_k):

$$I_{kk'} = \lambda_k^{-1/2} \exp\left(-i \lambda_k \rho_n\right) \delta_{kk'} \tag{26}$$

$$O_{kk'} = \lambda_k^{-1/2} \exp\left(i \lambda_k \rho_n\right) \delta_{kk'} \tag{27}$$

$$\lambda_k = \sqrt{W_{kk}}. \tag{28}$$

The probability matrix elements are defined according to the square modulus of the sector-dependent scattering matrix elements:

$$P^J_{kk'}(E;n) = |S^J_{kk'}(E;n)|^2. \tag{29}$$

Nonreactive transitions can be eliminated from the probability matrix by identifying reactant and product states via the expectation value of the hyperangle, $\langle\delta\rangle_k$, calculated in the basis of the δ-dependent wavefunctions:

$$\langle\delta\rangle_k = \sum_{i=1}^{3}\langle\Phi_i\psi_{(i,\nu)}|\hat{\delta}|\Phi_i\psi_{(i,\nu)}\rangle \tag{30}$$

$$= \sum_{i=1}^{3}\langle\Phi_i|\Phi_i\rangle \sum_{j,j'=1}^{N_\delta} c_j^{(i,\nu)}c_{j'}^{(i,\nu)}\langle\chi_j|\hat{\delta}|\chi_{j'}\rangle \tag{31}$$

$$= \sum_{i=1}^{3}\sum_{j,j'=1}^{N_\delta} c_j^{(i,\nu)}c_{j'}^{(i,\nu)}\langle\chi_j|\hat{\delta}|\chi_{j'}\rangle. \tag{32}$$

The probability of a reactive transition from initial reactant state $s = (i,\nu)$ to final product state $s' = (i,\nu)'$ is given by the probability matrix element $P^J_{ss'}(E;n)$, which is taken to be an average over a number of asymptotic matrix elements:

$$P^J_{ss'}(E) = \overline{P^J_{ss'}(E;n)}. \tag{33}$$

B. Dynamics

The $J = 0$ cumulative reaction probability (CRP) is defined as the sum of the state-to-state partial wave probabilities over all quantum states:

$$P_c^{J=0}(E) = \sum_s\sum_{s'} P_{ss'}^{J=0}(E). \tag{34}$$

The integral cross section (σ) provides a measure of reactivity by predicting the effective size of its molecular components[85] and has units of area.[85–87] The initial state selected integral reaction cross section, $\sigma_s(E_c^s)$, calculated as a function of collision energy ($E_c^s = E - \varepsilon_s$) is

$$\sigma_s(E_c^s) = \frac{\pi}{q_s^2}\sum_{s'}\sum_{J=0}^{J_{\max}}(2J+1)P_{ss'}(E), \tag{35}$$

where the squared initial translational wavenumber, q_s^2, is

$$q_s^2 = 2\mu_R(E - \varepsilon_s), \tag{36}$$

and where the reduced mass is $\mu_R = m_{\mathrm{Cl}}m_{\mathrm{CH_4}}/m_{\mathrm{total}}$ for reaction (2), and $\mu_R = m_{\mathrm{HCl}}m_{\mathrm{CH_3}}/m_{\mathrm{total}}$ for reaction (1). Provided initial populations of internal reactant states (a, b, ...) are known, the total cross section can be calculated[88] as

$$\sigma_{\mathrm{tot}} = a\sigma_0(E_c^0) + b\sigma_1(E_c^1) + \dots\ . \tag{37}$$

The nonadiabatic branching ratios can be determined by the ratio of final-state selected to total cross sections.

Collision time delay analysis affords an approximate method of interpreting whether features present in the cumulative reaction probability pertain to resonances in the reaction process, and is computed according to

$$\Delta t^J(E) = \frac{1}{P_c^J(E)}\sum_{s's} Re\left[S^J_{s's}(E)^*\left(-i\hbar\frac{d}{dE}\right)S^J_{s's}(E)\right],$$

where the asterisk signifies complex conjugate. Resonances are identified as positive maxima on a plot of collision time delay as a function of energy, relative to the time-delay baseline.[89,90]

C. Kinetics

Energy and J-shifting methods are used to calculate the RD thermal rate constant, $k(T)$, such that it can be expressed as a product of the TS rotational and (spectator mode) vibrational partition functions with the $J = 0$ thermal rate constant:[91]

$$k(T) = Q_{\mathrm{vib}}^{\mathrm{TS}}Q_{\mathrm{rot}}^{\mathrm{TS}}k^{J=0}(T) \tag{38}$$

$$= \frac{Q_{\mathrm{TS}}(T)}{hQ_{\mathrm{react}}(T)Q_{\mathrm{trans}}^{\mathrm{rel}}(T)}\int_0^\infty dE\ P_c^{J=0}(E)\ e^{-E/k_BT},$$

where h is Planck's constant, k_B is the Boltzmann constant, $Q_{\mathrm{trans}}^{\mathrm{rel}}(T)$ is the relative translational partition function and where the partition functions for the reactants ($Q_{\mathrm{react}}(T)$) and TS (Q_{TS}) are the product of vibrational, rotational, and electronic partition functions as specified in previous reports.[11,55] The electronic partition function for the Cl atom is $Q_{\mathrm{elec}} = 4 + 2\mathrm{e}^{-\Delta\mathrm{E_{SOC}}/k_BT}$.

The transition state theory (TST) thermal rate constant – which neglects quantum effects such as tunneling as well as recrossing dynamics[87] – is defined according to

$$k(T) = \frac{k_BT}{h}\frac{Q_{\mathrm{TS}}(T)}{Q_{\mathrm{react}}(T)Q_{\mathrm{trans}}^{\mathrm{rel}}(T)}e^{-V_0/k_BT}, \tag{39}$$

where V_0 is the vibrationally corrected *ab initio* barrier height. For calculation of the TST rate constant for the reverse reaction, we adjust the zero of energy to take into account the asymptotic lowering of the adiabatic potential by 1/3 of the spin-orbit coupling splitting, such that the argument of the exponent in equation (39) is $-(V_0 + \Delta\mathrm{E_{SOC}}/3)/k_BT$.

D. Numerical details

Single surface ($V_{\mathrm{A_1}}^{\mathrm{ad}}$) and multi-surface scattering calculations were performed for the forward and reverse reaction processes. As it was not necessary to distinguish between the asymptotically degenerate $\mathrm{Cl} + \mathrm{CH_4}$ states,

Table VII. Scattering numerical parameters[a].

	Description	Final Value
E_{inc}	Energy grid spacing	0.0001 eV
ρ_{min}	First ρ sector (behind TS)	8 au
ρ_{max}	Final asymptotic ρ sector	16 au
N_δ	Size of DVR basis	200
E_{max}	Maximum incident KE	1.4 (2.4) eV
N	Contracted basis size	20 (35)
N_{ad}	Contracted basis size (adiabatic)	10
N_ρ	Number of ρ sectors	750
S_{num}	Number of ρ sectors to average $P_{ss'}$	100
J_{max}	Maximum angular momentum	300

[a] Numbers in parentheses indicate parameters for high energy calculations required to compute the total cross section up to 1.3 eV.

symmetrized wavefunctions were not implemented. Convergence of cumulative reaction probabilities, hyperspherical adiabat energies, and cross sections were monitored with respect to the scattering parameters in Table VII. For $J > 0$ calculations a reduced energy grid spacing of 0.001 eV was used for computational efficiency.

V. SINGLE-SURFACE SCATTERING RESULTS

As nonadiabatic effects have previously been shown to have little effect on bimolecular rate constants[93] and the low energy multi-state CRP is dominated by electronically adiabatic transitions (Figure 7(a)), rate constants for forward and reverse reactions $CH_3 + HCl \rightleftharpoons CH_4 + Cl(^2P_{\frac{3}{2}})$ were calculated by scattering on $V^{\text{ad}}_{A_1}$. TST rate constants were estimated using the vibrationally corrected IB barrier height. The forward thermal rate constant for the IB surface compares favorably to experimental data[94–96] and provides significant improvement upon the low-temperature CUS/μOMT results of Rangel, et al.[7] (Figure 5a).

Thermal rate constants for the reverse reaction were calculated for the IB and Q//T surfaces and compared to experimental[97–100] and evaluated[95] kinetic data, as well as previous theoretical results[7,11,13] (Figure 5b). Using the highest level of *ab initio* theory to compute the surfaces (IB) resulted in thermal rate constants in excellent agreement with experimental results, though slightly larger than experiment at low temperatures. By contrast, the Q//T surface produces thermal rate constants much lower than experiment, thus indicating that higher-order basis sets are necessary for accurately describing this system. In addition, the difference between TST and more accurate calculations at high temperature could indicate the importance of recrossing effects in this HLH reaction. The forward and reverse thermal rate constants for the IB surface are given in Table VIII.

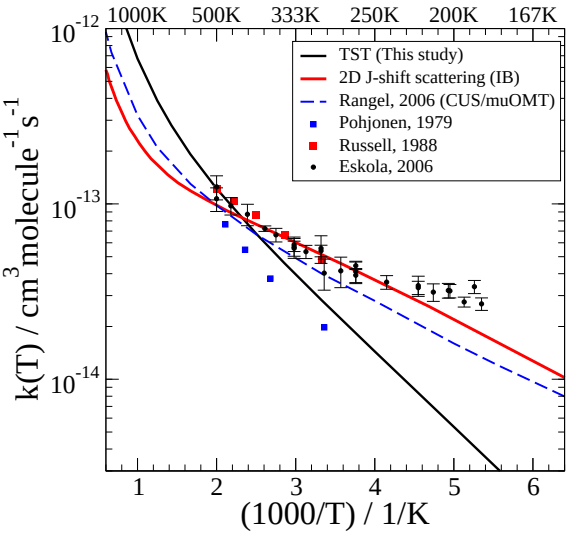

(a)$CH_3 + HCl \rightarrow CH_4 + Cl$

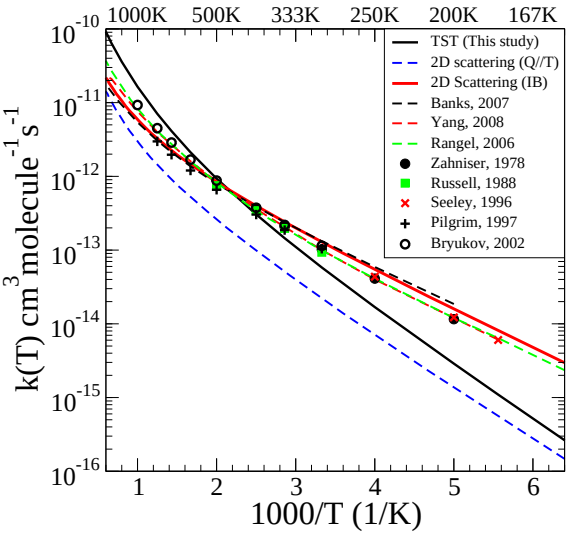

(b)$CH_4 + Cl \rightarrow CH_3 + HCl$

Figure 5. J-shifted thermal rate constants on the adiabatic ground state surfaces $V^{\text{ad}}_{A_1}$. (a) Forward reaction, for the IB surface. (b) Reverse reaction, for IB and Q//T surfaces. TST computed from IB *ab initio* energies.

VI. MULTI-SURFACE SCATTERING RESULTS

A. Hyperspherical adiabats

Hyperspherical adiabats for multi-surface scattering are shown in Figure 6, grouped according to vibrational excitation. Electrovibrational states $s = (i, \nu)$ (the ν^{th} vibrational level of the i^{th} electronic state) are identified by comparison with the asymptotic hyperspherical adiabats from scattering on the three adiabatic surfaces (not

Table VIII. Theoretical thermal rate constants for CH_3 + HCl $\rightleftharpoons$ CH_4 + Cl ($^2P_{\frac{3}{2}}$) on $V_{A_1}^{ad}$ (IB). Rates given in cm^3 molecule^{-1} s^{-1}; powers of ten shown in parentheses.

T / K	Forward	Reverse
250	3.70(-14)	5.45(-14)
300	5.14(-14)	1.28(-13)
350	6.45(-14)	2.42(-13)
400	7.64(-14)	3.98(-13)
500	9.81(-14)	8.39(-13)
600	1.19(-13)	1.46(-12)
800	1.67(-13)	3.26(-12)
1000	2.29(-13)	5.92(-12)
1500	4.72(-13)	1.69(-11)
2000	8.62(-13)	3.42(-11)

shown). Hyperspherical adiabats pertaining to electronic quantum numbers $i = 0, 1$, and 2 asymptotically correlate to adiabatic electronic states A_1, E_{low} and E_{high}, respectively. In the Cl + CH_4 channel, the ground $i = 0$ and 1 electronic states are degenerate (indistinguishable) while the $i = 2$ spin-orbit excited state falls much higher in energy. In the HCl + CH_3 channel (R), only ground state $i = 0$ hyperspherical adiabats are accessible, falling between the electronic ground and excited state product hyperspherical adiabats. The notation $s = (i, \nu)$ is thus dropped for (R) states where the vibrational quantum number ($\nu = 0, 1, \ldots$) alone specifies the state. For clarity of analysis in the Cl+CH_4 channel, the vibronic quantum number is redefined as $s = (q, \nu)$ such that $q = \frac{1}{2}$ identifies Cl* + CH_4 states and $q = \frac{3}{2}$ represents the sum over the degenerate Cl + CH_4 states $i = 0, 1$. In the CH_3 + HCl channel, the vibrational quantum number ($\nu = 0, 1, \ldots$) approximately pertains to the H–Cl stretch, whereas the vibrational quantum number in the Cl + CH_4 channel correlates to a C–H stretch.

B. Geometry of nonadiabatic transitions

A major advantage of hyperspherical coordinates is the ability to analyze reactive transitions in terms of hyperspherical adiabat avoided crossings in the vicinity of the potential ridge, defined as the dividing line between the reactant and product valleys.[101,102] A series of complex avoided crossings take place near the potential ridge (Figure 6), especially between the reactant R and the product Cl* states (e.g. $\rho = 11.64$ au / 0.321 eV and $\rho = 12.2$ au / 0.598 eV). It is likely that these avoided crossings pertain to (vibronic) nonadiabatic transitions.

The magnitude of the $q = \frac{1}{2}$ diabatic state wavefunction ($|\Psi^d_{\frac{1}{2},\nu}|^2$) indicates the location of nonadiabatic transition in the Cl+CH_4 channel. For each ν, the wavefunction probability begins with a sharp peak approximately coinciding with the location of the hyperspherical adiabat avoided crossings. The average geometries associated with the onset of diabatic wavefunction amplitudes are given in Table IX. Nonadiabatic transition is shown to occur at larger H–Cl separation with increasing vibrational excitation, indicating that H–Cl stretch excitation makes transition between electronic states possible at larger distances.

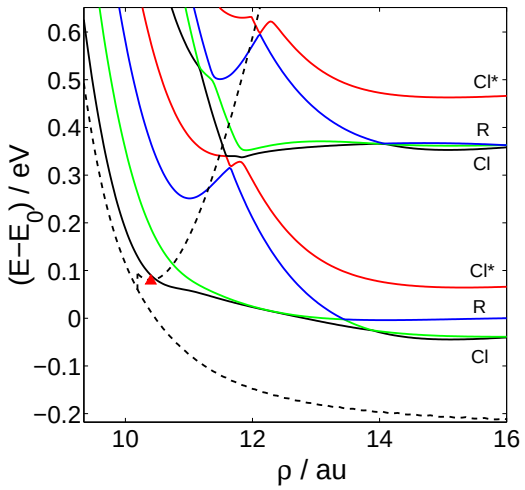

Figure 6. The eight lowest hyperspherical adiabats for the HCl + CH_3 $\rightleftharpoons$ Cl + CH_4 reaction. Quantum states $s = (i, \nu)$ are asymptotically grouped in terms of vibrational quantum number ν. Asymptotic electronic states are A_1: Cl ($^2P_{\frac{3}{2}}$) + CH_4 (solid black), E: Cl ($^2P_{\frac{3}{2}}$) + CH_4 (green), HCl + CH_3 (blue, R) and E: Cl* ($^2P_{\frac{1}{2}}$) + CH_4 (red). Potential ridge and minimum energy path along Cl + CH_4 channel are given as black dashed lines; TS location indicated by red triangle.

Table IX. Approximate location of nonadiabatic transition for the HCl + CH_3 $\rightarrow$ Cl* + CH_4 reaction.

State	ρ / au	δ / rad	R / Å	r(H–Cl) / Å	∼C–H / Å
TS	10.3925	0.1565	2.8509	1.4825	1.3684
$q, \nu = \frac{1}{2}, 0$	11.6181	0.1971	3.1641	2.0823	1.0817
$q, \nu = \frac{1}{2}, 1$	12.0603	0.1994	3.2830	2.1865	1.0965
$q, \nu = \frac{1}{2}, 2$	12.4623	0.2007	3.3915	2.2739	1.1176
$q, \nu = \frac{1}{2}, 3$	12.8643	0.2017	3.5002	2.3588	1.1414

C. $CH_3 + HCl \rightarrow CH_4 + Cl(^2P)$.

a. Reaction probabilities. The $J = 0$ CRP for the reaction (1) is shown in Figure 7(a). Oscillating reactivity typical of HLH systems[65] is observed, especially at low total energies. It is a dominant feature for the $\nu = 0$ and $\nu = 1$ initial state selected reaction probabilities. Resonances are also seen to play a significant role in the reaction process; $J = 0$ resonances are confirmed by the presence of peaks in time delay analysis

(Figure 7(b)). The contribution of the nonadiabatic reaction $HCl+CH_3 \rightarrow Cl^* + CH_4$ to the CRP is also shown in Figure 7(a). The onset of the nonadiabatic pathway is delayed relative to the electronically adiabatic pathway on this total energy scale. Furthermore, the onset coincides with resonances confirmed by time delay analysis, that are associated with nonadiabatic state-to-state probabilities. This could indicate a mechanism of resonance mediated nonadiabatic transition.

Initial state selected probability branching ratios ($\sum_{\nu'} P^{J=0}_{\nu\rightarrow(\frac{1}{2},\nu')}/P^{J=0}_c$) afford an estimate of the contribution of specific initial vibrational quantum states (ν) to nonadiabatic reaction. These ratios generally increase with energy (although some oscillation, especially for the $\nu = 0$ and $\nu = 1$ states, is present), indicating that approximately 4–6% ($\nu = 0$), 6-13% ($\nu = 1$), 20% ($\nu = 2$), and 25% ($\nu = 3$) of the reaction probability arises due to nonadiabatic production of Cl* at high energies. State-to-state reaction probabilities show that, with the exception of reaction from $\nu = 0$, electronically nonadiabatic transitions are generally associated with the loss of one quantum of stretch excitation:

$$HCl\ (\nu = n)\ +\ CH_3\ \rightarrow\ Cl^*\ +\ CH_4\ (\nu = n - 1).$$

For reactions from $\nu = 1$, the vibrationally adiabatic pathway also plays a large role, and for higher energies additional pathways become available for all channels. Finally, $J > 0$ calculations showed the functional form of the CRP is preserved as the angular momentum increases, thereby indicating that J-shifting is a good approximation in these calculations.

b. Integral cross sections. The initial state-selected integral cross sections for $HCl + CH_3 \rightarrow Cl + CH_4$ are given in Figure 8 as a function of collision energy ($J_{max} = 300$). Vibrationally excited channels open quickly once a state becomes accessible, whereas there is a delay associated with the onset of the $\nu = 0$ pathway.

c. Nonadiabatic branching ratio. The nonadiabatic branching ratio is constructed on a collision energy scale in order to compare the extent of predicted nonadiabaticity to experiment. Initial state selected branching ratios for the nonadiabatic production of Cl* can be calculated for each initial vibrational state according to

$$\Gamma_\nu = \frac{\sum_{\nu'} \sigma_{\nu\rightarrow(\frac{1}{2},\nu')}}{\sum_{\nu'}\sum_q \sigma_{\nu\rightarrow(q,\nu')}}; \qquad (40)$$

these ratios are shown in Figure 9. The correlation between nonadiabatic reaction and HCl vibrational excitation is clear; the ground state reaction from $\nu = 0$ occurs only for higher collision energies, whereas vibrationally excited states result in large initial spikes in the branching ratio. These peaks result from the opening of the nonadiabatic pathway via resonance mechanisms prior

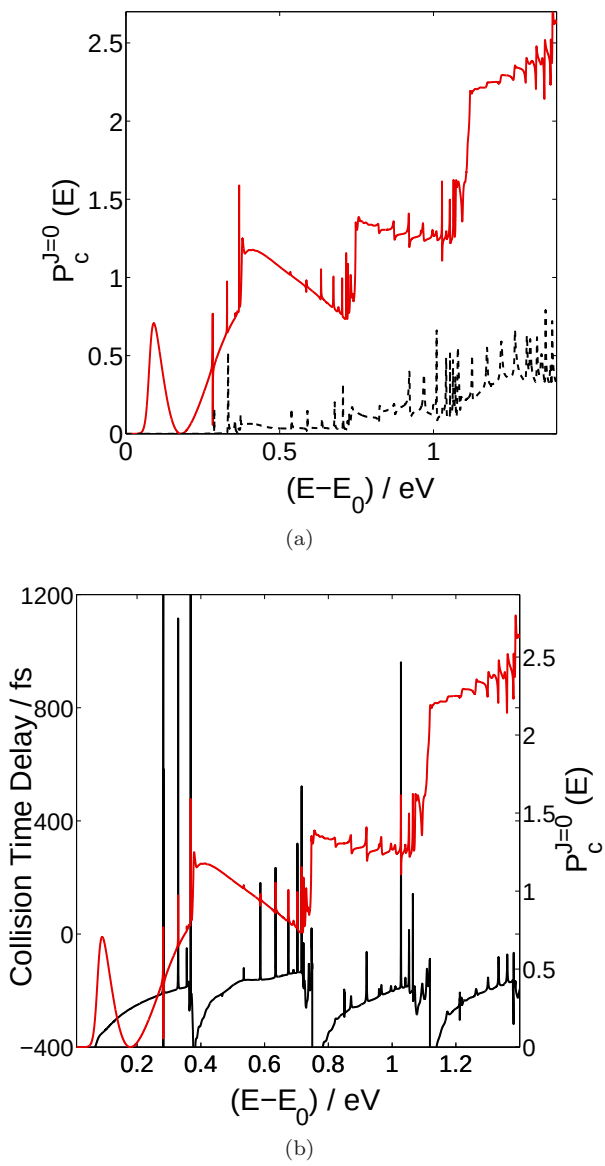

Figure 7. (a) $J = 0$ reaction probabilities for the $CH_3 + HCl \rightarrow CH_4 +$ Cl(^{2}P) reaction. CRP (red), nonadiabatic pathways (black, dashed). (b) Time delay analysis for identification of resonances (black). $J = 0$ CRP (red).

to the onset of the more dominant electronically adiabatic pathway. At high collision energies, the contribution of the nonadiabatic pathways levels out to between 4% ($\nu = 0$) to 22% ($\nu = 3$) of the total reactivity.

The experimental total nonadiabatic branching ratio was reported to be $\Gamma = 0.14 \pm 0.02$.[32] A total theoretical nonadiabatic branching ratio is constructed according to

$$\Gamma = \frac{\sum_{\nu'} \sigma_{\nu\rightarrow(\frac{1}{2},\nu')}}{\sigma_{tot}} \qquad (41)$$

and therefore requires knowledge of the initial populations of the $HCl + CH_3$ states. These populations have

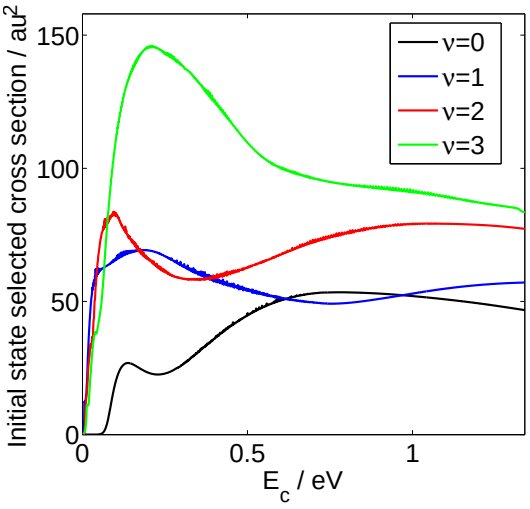

Figure 8. Initial state selected integral cross sections as a function of collision energy for reaction HCl(ν) $+CH_3 \rightarrow Cl + CH_4$.

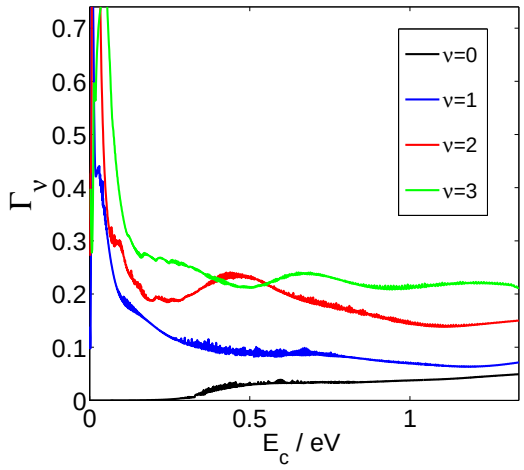

Figure 9. Initial state selected nonadiabatic branching ratio for HCl(ν) $+CH_3 \rightarrow$ Cl($^2P_{\frac{1}{2}}$) + CH_4

been measured experimentally;[103] the majority of internal energy is stored in the umbrella bending mode and the HCl reactant is vibrationally cold.[31] Direct comparison to experiment is difficult given that the current model does not account for umbrella bending vibration in the scattering calculations, describing instead the H–Cl stretching mode in the reactants. However, the correlation between vibrational excitation and nonadiabatic transition is clear even in this reduced dimensionality model, and therefore the approximation is made that the type of vibrational motion is not as significant as the amount of vibrational excitation available for reaction. The validity of this approximation is supported by previous studies highlighting the importance of intramolecular vibrational redistribution along the reaction path.[26]

Under the experimental conditions of reference,[31] a bimodal distribution of CH_3 radicals is present; the assumption is made here that only the fast channel (1.3 eV) contributes to nonadiabatic reaction,[31] with approximately $\langle E_{vib}^{exp} \rangle = 1100$ cm^{-1} of excess vibrational energy available to the CH_3 + HCl reactants.[103] The maximum vibrational excitation available to reactants, E_{vib}^{max}, was defined as 1.0, 1.5, 1.75 and 2.0 times the experimental quantity $\langle E_{vib}^{exp} \rangle$. Using the energies of the initial reactant states relative to the ground vibrational state, the populations of states $\nu = 0, 1, 2$, and 3 (governed by parameters a, b, c and d, respectively) were modeled to reproduce E_{vib}^{max} with the constraints that all parameters are positive and sum to one, and that the lower energy states are more populated than the high energy states ($a, b \geq c, d$). The results of this analysis are given in Table X.

Table X. Branching ratio model for nonadiabatic production of Cl*. Energies in cm^{-1}, branching ratio at 1.3 eV.

E_{vib}^{max}	a	b	c	d	Γ(%)
1100	0.808	0.064	0.064	0.064	7.6 %
1649	0.712	0.096	0.096	0.096	8.9 %
1924	0.664	0.112	0.112	0.112	9.4 %
2199	0.616	0.128	0.128	0.128	10.0 %
E (cm^{-1})	0	2928	5761	8492	

The models in Table X indicate approximately 7-10% contribution from the nonadiabatic reaction in comparison to the reported experimental branching ratio, 14±2%.[32] Vibrational energy in excess of experimentally measured values is required to bring these results into better agreement; this could indicate the importance of translation-vibration coupling along the reaction path. Alternately, it could indicate that additional degrees of freedom (such as the umbrella mode) must be treated with more accuracy in order to achieve quantitative comparison to experiment. Despite the additional vibrational energy required for these models, the correlation between model and experiment indicates that the reduced dimensionality, spin-orbit coupling model provides a good theoretical foundation from which to understand the electronic nonadiabatic transitions in this reaction system.

D. Cl (^2P_J) $+CH_4 \rightarrow$ HCl + CH_3.

The nonadiabatic properties of reaction (2) were also investigated, where it was evident that reaction from Cl* states plays a small but significant role. State-to-state reaction probabilities showed that reaction from Cl* was generally found to be associated with the release of one quantum of stretch excitation; resulting in the mechanism ($n = 1, 2$)

$$Cl^* + CH_4\ (\nu = n) \rightarrow HCl\ (\nu' = n{+}1) + CH_3.$$

The ground vibrational state reaction ($\nu = 0$), exhibited both vibrationally adiabatic ($\nu' = 0$) and nonadi-

abatic ($\nu' = 1$) pathways. These results are consistent with those reported in recent experiments by Wu et al.,[29] where it was noted that reaction of excited spin-orbit state Cl* was associated with production of stretch excited HCl ($\nu = 1$). Furthermore, release of one quantum of stretch excitation was also predicted to be a dominant pathway for the reaction of Br* + H_2.[45,46]

Integral cross section data also supported the assertion of the small, but significant contribution of the nonadiabatic pathway. Experimental data for the Cl* + $CH_4(\nu = 0)$[28] and Cl* + $CH_2D_2(\nu = 0)$[29] systems indicate the significant contribution of the nonadiabatic pathway, associated in both cases with the production of stretch excited HCl ($\nu = 1$) and mediated through a resonance pathway. The ratio of integral cross sections,

$$\sigma^*/\sigma_0 = \frac{\sum_{\nu'} \sigma_{(\frac{1}{2},0)\rightarrow\nu'}}{\sum_{\nu'} \sigma_{(\frac{3}{2},0)\rightarrow\nu'}}, \qquad (42)$$

was predicted to be 9% or larger for the Cl* + CH_2D_2 study of Wu and Liu[29] at 0.867 eV, depending upon the population of Cl* in the incident beam. We have determined this ratio to be 10.3% at 0.867 eV (Figure 10), which compares favorably with the experimental value, and to the predictions of previous X + H_2 studies.[35,37,40,41,44,46] The experimental threshold for the onset of reaction was reported to occur at 0.317 eV.[29] In the current study, reaction from Cl* + $CH_4(\nu = 0)$ opens at lower collision energies than the adiabatic pathway, as consistent with the conclusions of past theoretical studies,[41] but the electronically adiabatic reaction from Cl + $CH_4(\nu = 0)$ quickly dominates. Oscillating reactivity causes the ratio σ^*/σ_0 to decrease to nearly zero again before growing in at approximately 0.3 eV, in good agreement with the conclusions of Wu and Liu.[29] Vibrationally excited reactant states were found to produce higher nonadiabatic branching ratios.

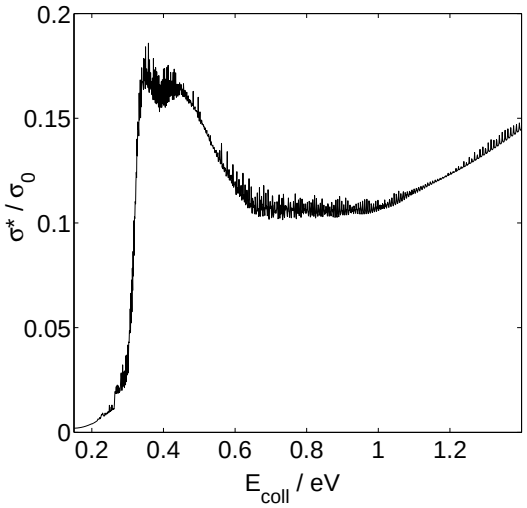

Figure 10. Ground state nonadiabatic cross section ratio for Cl* + $CH_4 \rightarrow$ HCl + CH_3.

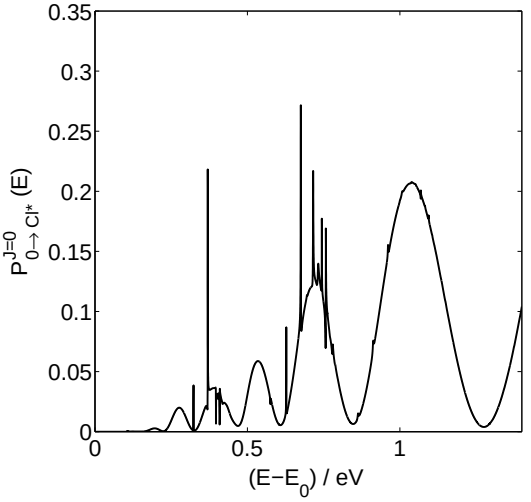

Figure 11. Nonreactive inelastic probability for the Cl + CH_4 ($\nu = 0$) →Cl* + CH_4 transition.

E. Nonreactive scattering.

Inelastic nonreactive scattering of Cl+$CH_4(\nu) \rightarrow$ Cl* + $CH_4(\nu')$ was also characterized, and is shown for the ground initial state $\nu = 0$ to all vibrational levels of the spin-orbit excited states (Cl* + CH_4) in Figure 11. The $\nu = 0$ inelastic scattering process is predominantly vibrationally adiabatic, whereas for $\nu = n,\ n > 0$, the most favorable nonadiabatic transition involves loss of one quantum of stretch excitation:

$$\mathrm{Cl} + \mathrm{CH_4}\ (\nu = n) \rightarrow \mathrm{Cl^*} + \mathrm{CH_4}\ (\nu' = \mathrm{n} - 1).$$

The loss of vibrational energy associated with nonadiabatic excitation was also previously reported for the Br + H_2 reaction system.[46] This result further indicates the importance of vibrational energy in mediating nonadiabatic transitions, as seen in the forward and reverse reaction processes. Furthermore, strong oscillatory reaction probability characteristic of HLH processes is observed, as consistent with previous studies.[36] Such behavior is potentially associated with interference effects arising from the two degenerate ground Cl electronic states.

VII. CONCLUSIONS

A reduced dimensional, multiple electronic surface model has been developed to provide a detailed and unified understanding of the ground and excited state properties of the forward and reverse HCl + $CH_3 \rightleftharpoons$ Cl + CH_4 reaction processes. Comparison to experiment provides a means of evaluating the relative importance of the approximations utilized in the current approach. The two dimensional surface system, consisting of three potentials and coupling terms between them, accurately reproduces

physical behavior; the diabatic states are degenerate in the Cl + CH_4 channel and the adiabatic states split by 852 cm^{-1}, in good agreement with experiment.

The TS was confirmed to be collinear as consistent with previous characterizations. The *ab initio* vibrationally corrected barrier heights at Q//T level of theory were found to be 2.78 kcal mol^{-1} and 3.57 kcal mol^{-1} and for reactions (1) and (2), respectively. Ground state IB thermal rate constants are in excellent agreement with experiment and, especially for reaction (1), provide an improved description in comparison to previously reported theoretical results.

Coupling between the active modes and the umbrella bending mode was evident from frequency projection, as consistent with the conclusions of past studies.[24,27] The close correlation between the ground state thermal rate constants and experiment indicates that despite this coupling, a two dimensional approximation is an effective simplification. The curvilinear projection method was found to be more accurate than its rectilinear counterpart in describing post-projected frequencies; unlike in previous studies,[50,51,55] a small number of imaginary frequencies were still observed post-projection.

The nonadiabatic transition occurs in the Cl + CH_4 reaction channel. The approximate location of nonadiabatic transition was also found to be dependent upon vibrational excitation; H–Cl bond lengths were seen to vary between 1.48–2.35 Å for final vibrational states $\nu = 0-3$. Larger vibrational excitation allows nonadiabatic transition to occur for increased values of molecular separation. This location of nonadiabatic transition supports the two-step reaction mechanism model;[43] electronic relaxation (or excitation) is followed (or preceded) by reaction on the ground state surface.

Strong resonance features were observed in state-to-state nonadiabatic reaction probabilities and confirmed by time-delay analysis. Some resonances were associated with the opening of the nonadiabatic pathway, causing a dominant contribution from nonadiabatic pathways at low collision energies for reaction (1). The importance of resonance features in the nonadiabatic reaction of Cl* + CH_4 was also reported by Wu et al.,[29] where it was hypothesised that nonadiabatic relaxation to produce the $\nu = 1$ vibrationally excited state was followed by reaction through a ground state resonance pathway. In the current study, it is difficult to ascertain whether the resonance features are directly associated with the nonadiabatic transitions or occur separately on the ground state post (or pre) nonadiabatic transition.

The correlation between vibrational energy and nonadiabatic reaction reported in experiment[29] was witnessed for reactive forward, reverse, and nonreactive transitions. Reactive transitions of type:

$$Cl^* + CH_4\ (\nu = n) \rightarrow HCl\ (\nu' = n{+}1) + CH_3$$

were found to dominate the reverse reaction mechanism ($n = 1, 2$). The ground state $\nu = 0$ reaction also exhibited this behavior, but additionally possessed a significant vibrationally adiabatic component. This behavior was also clear for reaction (1), where the nonadiabatic production of spin-orbit excited product states was associated with the loss of one quantum of stretch excitation. This mechanism was dominant for ($n > 0$):

$$HCl + CH_3\ (\nu = n) \rightarrow Cl^* + CH_4(\nu' = n{-}1).$$

A vibrationally adiabatic pathway was also found to be significant for the $n = 1$ transition. Nonreactive, nonadiabatic production of Cl* also exhibited vibrational energy dependence; excitation of ground Cl to excited state Cl* was generally associated with the release of one quantum of vibrational energy, with the obvious exception of the ground state transition. The dominant pathway was thus observed to be ($n > 0$):

$$Cl + CH_4\ (\nu = n) \rightarrow Cl^* + CH_4\ (\nu' = n - 1)$$

Nonadiabatic pathways for the forward reaction were found to account for between approximately 7-10% of reactivity for reaction (1), in comparison to the $14 \pm 2\%$ predicted by experiment.[32] The comparison is approximate; more vibrational energy than available to experiment is required in order to achieve quantitative agreement. This could indicate that coupling of translation into vibrational motion plays an important role or that the 2D approach needs to be extended to more dimensions to completely describe the nonadiabatic pathway. Regardless, the model provides qualitative agreement with experiment regarding the extent of nonadiabaticity. Conversely, the description of reaction (2) did afford quantitative comparison; the ratio σ^*/σ_0 was reported to be 10.3%, in excellent agreement with the experimental value of 9% for reaction Cl + CH_2D_2.[29]

ACKNOWLEDGMENTS

This work was supported by the Engineering and Physical Sciences Research Council (Grant No. EP/G00224X/1) and the United States Office for Naval Research (Grant No. N00014-05-1-0460). S.M.R. acknowledges the Oxford University Press for receipt of a Clarendon Scholarship. Calculations were run in part using the Oxford Supercomputing Centre resources. We would like to thank Dr. Frank von Horsten, Dr. Ivan Ljubić, Dr. Stuart Greaves, Dr. Rebecca Rose, Professor Joel Bowman and Professor Kopin Liu for useful discussions.

REFERENCES

[1] A. R. Douglass, M. R. Schoeberl, R. S. Stolarski, J. Waters, J. M. Russell, A. E. Roche, and S. T. Massie, J. Geophys. Res. **100**, 13967 (1995).

[2]H. A. Michelsen, C. Webster, G. Manney, D. Scott, J. Margitan, R. May, R. Irion, M. Gunson, J. Russell, and C. Spivarkovsky, J. Geophys. Res. **104**, 26419 (1999).
[3]M. Sanee, L. Froidevaux, G. Manney, W. Read, J. Waters, M. Chipperfield, A. Roche, J. Kumer, J. Mergenthaler, and J. Rusell, J. Geophys. Res. **101**, 18835 (1996).
[4]M. Prather and A. H. Jaffe, J. Geophys. Res. **95**, 3473 (1990).
[5]N. Tanaka, Y. Xiao, and A. C. Lasaga, J. Atmos. Chem. **23**, 37 (1996).
[6]Y. Wu and Y.-F. Lin, Combust. Flame **137**, 376 (2004).
[7]C. Rangel, M. Navarrete, J. C. Corchado, and J. Espinosa-García, J. Chem. Phys. **124**, 124306 (2006).
[8]T. N. Truong, D. G. Truhlar, K. K. Baldridge, M. S. Gordon, and R. Steckler, J. Chem. Phys. **90**, 7137 (1989).
[9]D. Troya, J. Millán, I. Banos, and M. González, J. Chem. Phys. **117**, 5730 (2002).
[10]J. F. Castillo, F. J. Aoiz, and L. Banares, J. Chem. Phys. **125**, 124316 (2006).
[11]S. T. Banks and D. C. Clary, Phys. Chem. Chem. Phys. **9**, 933 (2007).
[12]Z. Zhou, G. Chen, X. Zhou, and H. Fu, Int. J. Quantum Chem. **87**, 49 (2002).
[13]M. Yang, C.-L. Yang, J. Chen, and Q. Zhang, Chem. Phys. **354**, 180 (2008).
[14]W. R. Simpson, T. P. Rakitzis, S. A. Kandel, T. Lev-On, and R. N. Zare, J. Phys. Chem. **100**, 7938 (1996).
[15]H. A. Michelsen, Acc. Chem. Res. **34**, 331 (2001).
[16]X. Wang, M. Ben-Nun, and R. Levine, Chem. Phys. **197**, 1 (1995).
[17]R. Martínez, M. González, P. Defazio, and C. Petrongolo, J. Chem. Phys. **127**, 104302 (2007).
[18]H. A. Michelsen and W. R. Simpson, J. Phys. Chem. A **105**, 1476 (2001).
[19]A. Teslja and J. J. Valentini, J. Chem. Phys. **125**, 132304 (2006).
[20]A. J. Orr-Ewing, W. R. Simpson, T. P. Rakitzis, S. A. Kandel, and R. N. Zare, J. Chem. Phys. **106**, 5961 (1997).
[21]G. Nyman, J. Zhou, B. Zhang, and K. Liu, Isr. J. Chem. **47**, 1 (2007).
[22]J. Zhou, B. Zhang, J. J. Lin, and K. Liu, Mol. Phys. **103**, 1757 (2005).
[23]W. T. Duncan and T. N. Truong, J. Chem. Phys. **103**, 9642 (1995).
[24]J. C. Corchado, D. G. Truhlar, and J. Espinosa-Garcia, J. Chem. Phys. **112**, 9375 (2000).
[25]H.-G. Yu and G. Nyman, J. Chem. Phys. **110**, 7233 (1999).
[26]J. Sansón, J. C. Corchado, C. Rangel, and J. Espinosa-Garcia, J. Chem. Phys. **124**, 074312 (2006).
[27]J. Espinosa-Garcia and J. C. Corchado, J. Chem. Phys. **105**, 3517 (1996).
[28]B. Zhang and K. Liu, J. Chem. Phys. **122**, 101102 (2005).
[29]Y.-T. Wu and K. Liu, J. Chem. Phys. **129**, 154302 (2008).
[30]B. Retail, J. K. Pearce, C. Murray, and A. J. Orr-Ewing, J. Chem. Phys. **122**, 101101 (2005).
[31]B. Retail, S. J. Greaves, J. K. Pearce, R. A. Rose, and A. J. Orr-Ewing, Phys. Chem. Chem. Phys. **9**, 3261 (2007).
[32]B. Retail, J. K. Pearce, S. J. Greaves, R. A. Rose, and A. J. Orr-Ewing, J. Chem. Phys. **128**, 184303 (2008).
[33]R. A. Rose, S. J. Greaves, and A. J. Orr-Ewing, Mol. Phys. **108**, 981 (2010).
[34]K. Liu, Annu. Rev. Phys. Chem. **52**, 139 (2001).
[35]X. Wang, W. Dong, C. Xiao, L. Che, Z. Ren, D. Dai, X. Wang, P. Casavecchia, X. Yang, B. Jiang, et al., Science **322**, 573 (2008), http://www.sciencemag.org/cgi/reprint/322/5901/573.pdf.
[36]M. H. Alexander, G. Capecchi, and H.-J. Werner, Science **296**, 715 (2002).
[37]N. Balucani, D. Skouteris, L. Cartechini, G. Capozza, E. Segoloni, P. Casavecchia, M. H. Alexander, G. Capecchi, and H.-J. Werner, Phys. Rev. Lett. **91**, 013201 (2003).
[38]N. Balucani, D. Skouteris, G. Capozza, E. Segoloni, P. Casavecchia, M. H. Alexander, G. Capecchi, and H.-J. Werner, Phys. Chem. Chem. Phys. **6**, 5007 (2004).
[39]M. H. Alexander, G. Capecchi, and H.-J. Werner, Faraday Discuss. **127**, 59 (2004).
[40]M. H. Alexander, H.-J. Werner, and D. E. Manolopoulos, J. Chem. Phys. **109**, 5710 (1998).
[41]M. H. Alexander, D. E. Manolopoulos, and H.-J. Werner, J. Chem. Phys. **113**, 11084 (2000).
[42]Y.-R. Tzeng and M. H. Alexander, J. Chem. Phys. **121**, 5812 (2004).
[43]B. Lepetit, J. M. Launay, and M. L. Dourneuf, Chem. Phys. **106**, 111 (1986).
[44]C. S. Maierle, G. C. Schatz, M. S. Gordon, P. McCabe, and J. N. L. Connor, J. Chem. Soc., Faraday Trans. **93**, 709 (1997).
[45]S. L. Mielke, D. G. Truhlar, and D. W. Schwenke, J. Phys. Chem. **99**, 16210 (1995).
[46]T. Takayanagi and Y. Kurosaki, J. Chem. Phys. **113**, 7158 (2000).
[47]K. Yagi, T. Takayanagi, T. Taketsugu, and K. Hirao, J. Chem. Phys. **120**, 10395 (2004).
[48]R. B. Walker and E. F. Hayes, in *The Theory of Chemical Reaction Dynamics*, edited by D. Clary (D. Reidel Publishing Company, Dordrecht, 1985), p. 105.
[49]B. Kerkeni and D. C. Clary, J. Chem. Phys. **120**, 2308 (2004).
[50]S. T. Banks and D. C. Clary, J. Chem. Phys. **130**, 024106 (2009).
[51]S. T. Banks, C. S. Tautermann, S. M. Remmert, and D. C. Clary, J. Chem. Phys. **131**, 044111 (2009).
[52]B. Kerkeni and D. C. Clary, Mol. Phys. **103**, 1745 (2005).

[53]B. Kerkeni and D. C. Clary, Chem. Phys. Lett. **438**, 1 (2007).
[54]B. Kerkeni and D. C. Clary, J. Phys. Chem. A **107**, 10851 (2003).
[55]S. M. Remmert, S. T. Banks, and D. C. Clary, J. Phys. Chem. A **113**, 4255 (2009).
[56]H. F. von Horsten and D. C. Clary, Phys. Chem. Chem. Phys. **13**, 4340 (2011).
[57]A. W. Jasper, C. Zhu, S. Nangia, and D. G. Truhlar, Faraday Discuss. **127**, 1 (2004).
[58]A. P. Hickman, Int. Rev. Phys. Chem. **16**, 177 (1997).
[59]V. Aquilanti, S. Cavalli, D. De Fazio, and A. Volpi, Int. J. Quantum Chem. **85**, 368 (2001).
[60]A. C. Stanton, Chem. Phys. Lett. **122**, 385 (1985).
[61]D. E. Manolopoulos, *State to State Reactive Scattering* (John Wiley & Sons, Ltd, 2002).
[62]A. Kuppermann, J. A. Kaye, J. P. Dwyer, Chem. Phys. Lett. **74**, 257 (1980).
[63]L. M. Delves, Nucl. Phys. **9**, 391 (1958).
[64]L. M. Delves, Nucl. Phys. **20**, 275 (1960).
[65]J. Romelt, in *The Theory of Chemical Reaction Dynamics*, edited by D. C. Clary (D. Riedel Publishing Company, Dordrecht, 1985), p. 77.
[66]J. Palma and D. C. Clary, J. Chem. Phys. **112**, 1859 (2000).
[67]H.-J. Werner, P. J. Knowles, R. Lindh, F. R. Manby, M. Schütz, P. Celani, T. Korona, A. Mitrushenkov, G. Rauhut, T. B. Adler, et al., *Molpro, version 2008.3, a package of ab initio programs* (2008).
[68]D. J. Feller, Computational Chemistry **17**, 1571 (1996).
[69]K. Schuchardt, B. Didier, T. Elsethagen, L. Sun, V. Gurumoorthi, J. Chase, J.and Li, and T. Windus, J. Chem. Inf. Model **47**, 1045 (2007).
[70]A. Halkier, T. Helgaker, P. Jorgensen, W. Klopper, H. Koch, J. Olsen, and A. K. Wilson, Chem. Phys. Lett. **286**, 243 (1998).
[71]D. Troya and P. J. E. Weiss, J. Chem. Phys. **124**, 074313 (2006).
[72]*CRC Handbook of Chemistry and Physics, 78th ed.* (CRC Press, Inc., Boca Raton, FL., 1998).
[73]M. C. Jr, C. A. Davies, J. D. Jr., D. Frurip, and R. McDonald, eds., *ANAF Thermochemical Tables, 3rd Ed.* (Natl. Stand. Ref. Data Ser. Natl. Bur. Stand, Vol 14., 1985).
[74]D.-h. Lu and D. G. Truhlar, J. Chem. Phys. **99**, 2723 (1993).
[75]*Matlab, version 7.1.0.183 (r14) service pack 3* (2007).
[76]E. Stechel, R. B. Walker, and J. C. Light, J. Chem. Phys. **69**, 3518 (1978).
[77]D. E. Manolopoulos, J. Chem. Soc., Faraday Trans. **93**, 673 (1997).
[78]B. Lepetit, J. M. Launay, M. Le Dourneuf, and F. X. Gadia, Chem. Phys. **117**, 17 (1987).
[79]J. T. Muckerman, Chem. Phys. Lett. **173**, 200 (1990).
[80]J. M. Bowman and A. Wagner, in *The Theory of Chemical Reaction Dynamics*, edited by D. C. Clary (D. Riedel Publishing Company, Dordrecht, 1985), p. 47.
[81]J. C. Light, R. B. Walker, E. B. Stechel, and T. G. Schmalz, Comp. Phys. Comm. **17**, 89 (1979).
[82]A. N. Brooks and D. C. Clary, J. Chem. Phys. **92**, 4178 (1990).
[83]D. C. Clary, J. Chem. Phys. **95**, 7298 (1991).
[84]G. Nyman, H.-G. Yu, and R. B. Walker, J. Chem. Phys. **109**, 5896 (1998).
[85]R. D. Levine and R. B. Bernstein, *Molecular Reaction Dynamics and Chemical Reactivity* (Oxford University Press, 1987).
[86]M. S. Child, *Molecular Collision Theory* (Dover Publications, Inc., 1974).
[87]H. E. Henriksen and F. Y. Hansen, *Theories of Molecular Reaction Dynamics* (Oxford University Press, 2008).
[88]M. Brouard and C. Vallance, *Tutorials in Molecular Reaction Dynamics* (Royal Society of Chemistry, 2012).
[89]S. D. Chao and R. T. Skodje, J. Chem. Phys. **119**, 1462 (2003).
[90]J. F. Castillo, D. E. Manolopoulos, K. Stark, and H. J. Werner, J. Chem. Phys. **104**, 6531 (1996).
[91]J. M. Bowman, in *Reaction and molecular dynamics: proceedings of the European School on Computational Chemistry*, edited by A. Lagana (Springer, 1999), p. 101.
[92]U. Manthe, G. Capecchi, H.J. Werner, and H. J. Werner, Phys. Chem. Chem. Phys. **6**, 5026 (2004).
[93]G. C. Schatz, J. Phys. Chem. **99**, 7522 (1995).
[94]A. J. Eskola, J. A. Seetula, and R. S. Timonen, Chem. Phys. **331**, 26 (2006).
[95]J. J. Russell, J. A. Seetula, S. M. Senkan, and D. Gutman, Int. J. Chem. Kinet. **20**, 759 (1988).
[96]M.-L. Pohjonen and J. Koskikallio, Acta Chem. Scand. **33**, 449 (1979).
[97]M. S. Zahniser, B. M. Berquist, and F. Kaufman, Int. J. Chem. Kinet. **10**, 15 (1978).
[98]J. V. Seeley, J. T. Jayne, and M. J. Molina, J. Phys. Chem. **100**, 4019 (1996).
[99]J. S. Pilgrim, A. McIlroy, and C. A. Taatjes, J. Phys. Chem. A **101**, 1873 (1997).
[100]M. G. Bryukov, I. R. Slagle, and V. D. Knyazev, J. Phys. Chem. A **106**, 10532 (2002).
[101]A. Ohsaki and H. Nakamura, Phys. Rep. **187**, 1 (1990).
[102]D. C. Clary, J. Phys. Chem. **98**, 10678 (1994).
[103]G. Li, H. J. Hwang, and H. C. Jung, Rev. Sci. Instrum. **76**, 023105 (2005).